Analysis and Performance of an Ironless Stator Axial Flux PM Machine

N. F. Lombard, M. J. Kamper, Member, IEEE
Department of Electrical and Electronic Engineering
University of Stellenbosch, 7600 Stellenbosch, South Africa

***Abstract*—This paper presents the analysis, design and performance of an axial flux permanent magnet (AFPM) machine with an ironless stator. The topology has a large airgap length and zero core losses. A machine model that uses both lumped magnetic circuit and finite element method results is used with a multi-variable optimization algorithm to obtain the optimum machine dimensions. Special attention is given to the magnet interpolar gap to ensure a certain minimum plateau width for brushless DC operation. The large airgap length allows several approximations to be made that simplifies the machine model. A prototype machine is constructed and evaluated. Measured results of the armature reaction effect in the large airgap are given and discussed.**

***Keywords*—Axial flux, permanent magnet, ironless stator.**

I. Introduction

With high energy density NdFeB magnets, it is possible to attain a relatively high airgap flux density in large airgap machines with a small magnet volume. Topologies such as the slotless AFPM machine have consequently received an increased interest [1, 2, 3, 4]. Caricchi [5] also proposed a large torque density wheel direct drive AFPM machine with a water–cooled ironless stator.

This paper proposes an air-cooled ironless stator AFPM machine (Fig. 1) for high efficiency applications such as flywheels, wind generators and internal combustion machine generators. The zero core losses of the topology make very high efficiency at high speed possible, but the large airgap length requires a large volume of high field magnet to establish an adequate airgap flux density. The price of high field magnets is expected to decrease as production volume increases. Topologies that offer an increased efficiency at the cost of higher magnet volume may then be used in less specialized applications.

PE-234-EC-0-08-1998 A paper recommended and approved by the IEEE Electric Machinery Committee of the IEEE Power Engineering Society for publication in the IEEE Transactions on Energy Conversion. Manuscript submitted December 22, 1997; made available for printing August 14, 1998.

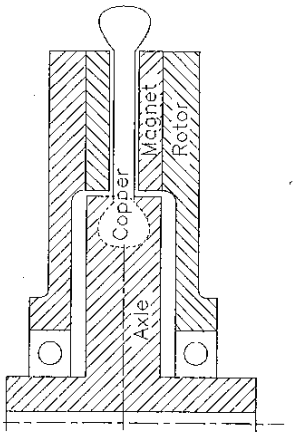

Fig. 1. Machine Topology

An analysis of the large airgap with trapezoidal stator windings is done in this paper in order to manipulate the shape of the induced phase emf and its plateau width by adjusting the angle that is left open between rotor magnets.

II. Design Method

A standard approach is followed in which a machine model is obtained that predicts the machine performances for a set of input dimensions. An algorithm that optimizes a single function of multiple variables searches for the set of inputs at which a selected performance parameter is at its maximum or minimum value. Penalty functions are used to keep other performance parameters at acceptable values.

A. The Machine Model

1) Lumped circuit analysis: Fig. 2 shows a section of the machine with its magnetic flux paths as seen from a

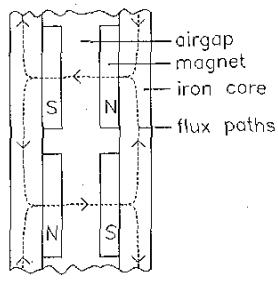

Fig. 2. Magnetic Flux Paths

radial direction, and Fig. 3 shows a lumped circuit model (LCM) corresponding to the area in Fig. 2. The large magnet and airgap lengths associated with the ironless stator topology cause the magnet and airgap reluctances (R_m and R_{ag}) to dominate the core reluctance R_c. For that reason the LCM may be used to obtain an accurate value for peak airgap flux density; that is the flux density in regions far removed from fringing effects. This is done by calculating R_{ag} with the airgap area set equal to the magnet pole area. The peak airgap flux density then is

$$B_{ag}(peak) = \left(\frac{4 \cdot R_m}{4 \cdot R_m + 4 \cdot R_{ag} + R_c}\right) \times B_r, \quad (1)$$

where B_r is the magnet remanence flux density.

The core permeability used to calculate R_c in (1) is initially determined by iteratively calculating the core flux density that satisfies both (1) and the core material's BH curve until the result converges sufficiently. During this process, an estimation of the increase in airgap area due to fringing is made when calculating R_{ag}; neglecting the fringing would result in a lower flux per pole than in reality.

2) The interpolar angle θ_{ip}: For every set of machine dimensions received from the optimization algorithm, the machine model determines the angle between the rotor magnets (θ_{ip} in Fig. 4) such that the emf induced in a phase at the start of its current conduction period is a specified percentage of its plateau value. This ensures

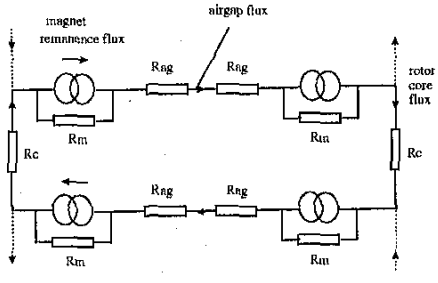

Fig. 3. Lumped Circuit Model

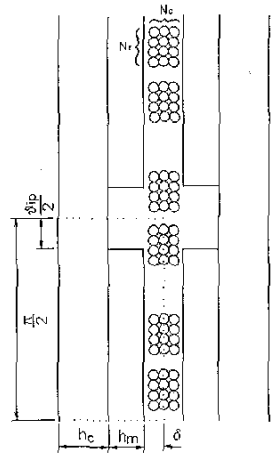

Fig. 4. FEM Region of Analysis

that the percentage emf dip at the instant of current commutation (and therefore the torque dip under current control) is fixed. It also ensures that the emf shape of all designs are the same and allows the optimization to be done in terms of the peak machine performance parameters (such as torque and power). This is very convenient as the peak performances may be calculated from the peak flux density obtained from the LCM.

3) FEM analysis: The machine model calculates the desired value of θ_{ip} as follows: a series of finite element method (FEM) analyses are carried out beforehand on machines with different dimensions. Each FEM analysis solves for the airgap flux density on a 2-D section taken midway between the magnets' inside and outside radii. The region of analysis is shown in Fig. 4. The analyses are done with zero stator current because the armature reaction effect in such a large airgap is expected to be small.

Fig. 5 shows the airgap flux density at different axial positions computed by the FEM. The axial variation is averaged, and the result (shown in a solid line) is fitted to a polynomial to obtain the flux density (B_{ag}) as a function of angular position (θ). The coil emf at rotor displacement position θ_d and at shaft speed ω is given by (2) in terms of $B_{ag}(\theta)$:

$$e_{coil}(\theta_d) = \omega(R_o^2 - R_i^2)N_c \sum_{n=1}^{N_r} B_{ag}(\theta_d - \frac{\theta_c}{2} + (\frac{n-1}{N_r - 1}).\theta_c). \quad (2)$$

R_i and R_o are the magnet inside and outside radius. Equation (2) is derived for a rectangular stator coil with N_r layers of conductors in the angular direction, spanning an angle of θ_c in total. Each layer has N_c conductors spread over the axial direction of the coil, so that

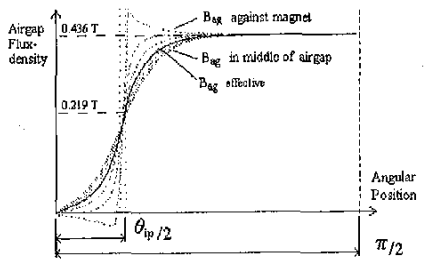

Fig. 5. Flux Density Distribution computed by FEM

the total number of coil turns is $N = N_r \times N_c$. This is shown in the uppermost coil of Fig. 4. The value of θ_c is taken as $\frac{\pi}{3}$ electrical radians, which is the maximum for a 3–phase machine. Fig. 6 shows the stator coil distribution as well as the emf waveform obtained by evaluating (2) at a number of different rotor positions. Fig. 6 also shows the rise angle. This is defined as the rotor angle displacement in which the induced emf rises from zero to a certain percentage, say χ percent, of its plateau value.

The series of FEM analyses are conducted to compute the emf shapes and subsequently the rise angles for machines with different dimensions. The machine model interpolates between this data [8] to find the magnet interpolar gap θ_{ip} for which the rise angle is $\frac{\pi}{6}$ electrical radians; that is because current conduction in a phase starts $\frac{\pi}{6}$ electric radians after the emf's zero crossing. The value of χ must be set to reach a compromise between low magnet cost and low torque ripple. The FEM solver and some graphics utilities are sourced directly from Hoole [6].

4) Summary: The actions taken by the machine model is summarized as follows:

- The machine model uses the FEM data to determine the angle θ_{ip} for the current set of machine dimensions that will result in an emf rise angle of $\frac{\pi}{6}$ radians.

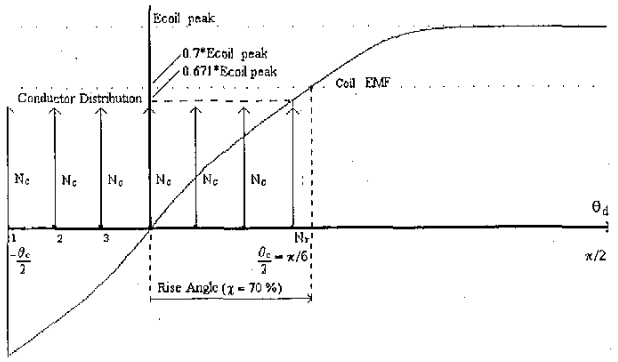

Fig. 6. Conductor Distribution & Stator Coil EMF

- It uses a lumped circuit model to compute the peak airgap flux density
- It determines the turns per coil and number of parallel paths that results in an induced stator emf at full speed that is less than the maximum converter voltage.
- The sizes and mass of the different machine components are calculated, and their material costs are approximated.
- The machine model determines the peak current density from the maximum allowable copper loss. It then calculates the torque peak that occurs in every electric cycle.
- The parameter to be optimized is selected as the machine model function. Other important parameters are maintained at acceptable values by imposing quadratic penalties on the function.

B. The Optimization Process

The variable metric (quasi-Newton) method is used to maximize or minimize the machine model function of multiple variables. The inverse Hessian approximation is updated with the *Broyden-Fletcher-Goldfarb-Shanno* algorithm [7].

As a case study, an AFPM machine is designed and constructed. The total material cost of a machine with outside magnet radius of 0.16 m is minimized subject to the constraints of an average torque larger than 26 Nm and a total axial length smaller than 100 mm. The machine is to be operated at 5500 r/min maximum from an inverter with a 600 V DC bus.

A value of 70% is assigned to the parameter χ. Experimentation with different designs has shown that with $\chi = 0.7$ the ratio of average to peak emf induced during the current conduction period is between 0.92 and 0.95. This translates the average torque requirement of 26 Nm to a peak torque of 28.3 Nm in the worst case. A quadratic penalty is imposed for $T < 30$ Nm, and for total weight $W > 35$ kg. The latter is to prevent the rotor core axial thickness from becoming very large.

Despite its lower active copper area, only a 3–phase machine is considered so as to keep the stator construction simple. Except for more phase-arms, a higher number of phases also requires a wider emf plateau width and consequently a larger magnet volume. A high number of pole pairs reduces end winding length and core thickness, but it requires a larger magnet volume to maintain the width of the emf plateau. For the machine size of the case study, four pole pairs were found to suit these extremes the best. Table I lists the machine parameters obtained for these penalties and constraints.

TABLE I
OPTIMIZED MACHINE PARAMETERS

Function $\longrightarrow$		Material Cost
Penalties/Constraints $\longrightarrow$		$T < 30$ Nm $W > 35$ kg R_o =0.16 $N_{phases} = 3$ $N_{poles} = 8$
Optimum Machine Variables		
R_i	[mm]	99.6
h_m	[mm]	5.0
δ	[mm]	7.0
B_{core}	[T]	1.12
Machine Characteristics		
θ_{ip}	[rad]	0.737
h_c	[mm]	18.2
N_{coil}		132
$a_{coil} \setminus a_{phase}$		$2 \setminus 8$
B_{ag}(peak)	[T]	0.438
I_{rated}	[A]	32.8
J_{peak}	[A/mm^2]	5.2
T_{rated}(peak)	[Nm]	29.6
E_{ph} @5500 rpm	[V]	259.9
W	[kg]	36.2
Material Cost	[R]	5464

A FEM analysis of the selected design shows the ratio of average emf in the current conduction period to peak emf as 0.942. From (3) the peak emf constant is 0.897, and the average emf constant is $0.897 \times 0.942 = 0.845$.

$$\frac{E_{ph}(peak)}{\omega} = \frac{N_{coil}N_{poles}}{2a_{phase}} B_{ag}(peak)(R_o^2 - R_i^2). \quad (3)$$

The average machine torque constant is also 0.845 as it is given by the same expression as the emf constant. Then

$$T_{max}(average) = 32.8 \times 0.845 = 27.7\,\text{Nm}.$$

III. CONSTRUCTION

Fig. 7 shows a scale drawing of a cross section through the axis of the constructed AFPM machine. The rotor discs are subjected to an axial force of 2800 N and are therefore supported with spacers on their outer sides. This requires the discs to extend beyond the end windings and contributes largely to the machine weight and inertia.

The stator windings (Fig. 8) are fixed into position by coating the whole unit with a high strength composite material. The seat that fits onto the axle is constructed by moulding the composite material and machining it to pressure fit on the axle. With proper curing, the heat distortion temperature of the composite material is 149° C. This is high enough considering the fact that the NdFeB magnets start to demagnetize at $\pm$ 120°C.

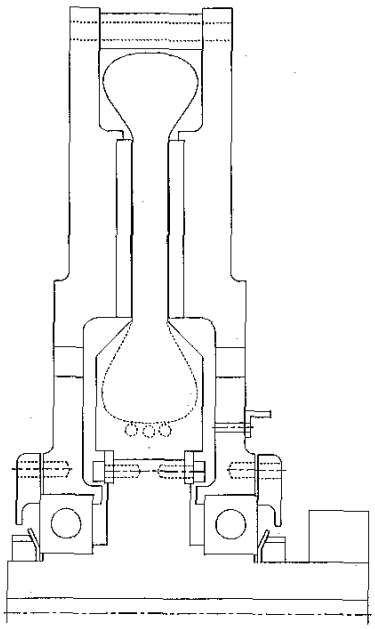

Fig. 7. Machine Section

The magnets are fixed to the rotor discs with a composite material that has a large lamination shear strength. A small edge is provided on the rotor discs to aid the composite material in withstanding centrifugal forces on the magnets..

IV. MEASURED RESULTS

Generator operation measurements were taken first to compare the shapes of the open circuit airgap flux density and phase emf with that predicted by the FEM. The machine efficiency and extent of armature reaction were also measured under generator operation.

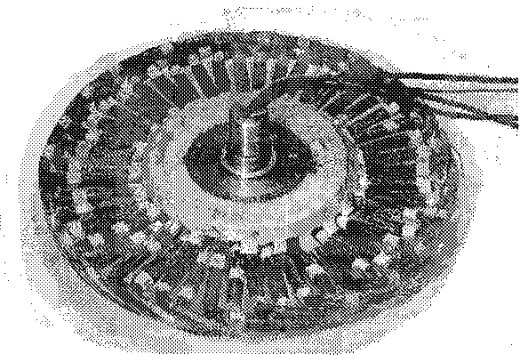

Fig. 8. Stator Windings

A. Generator Operation

A low speed (1500 rpm) DC machine was available for use as a mechanical source and a three phase resistor bank was used as load. Fig. 9 shows the flux density waveform (measured by a concentrated test coil) and the phase emf, both for zero stator current and at 101.6 rad/s. The relationship between voltage and flux density for the 10-turn test coil is

$$\begin{aligned} E_{test} &= N \times B_{ag} \times (R_o^2 - R_i^2) \times \omega_{shaft} \\ &= 15.85 B_{ag}. \end{aligned} \quad (4)$$

Table II compares the measured open circuit flux density and emf waveforms of Fig. 9 with the FEM computed flux density (Fig. 5) and emf (Fig. 6) at a few positions. The positions of comparison are relative to the zero crossing point of each trace. The voltages measured by the test coil is converted to flux density through (4).

TABLE II
COMPARISON OF MEASURED AND FEM RESULTS

	B_{ag} [T]		E_{ph} [V] at 970 rpm	
at position [rad] $\longrightarrow$	$\theta_{ip}/2$	$\pi/2$	$\pi/6$	$\pi/2$
FEM	0.219	0.436	30.56	45.55
Measured	0.227	0.434	29.38	45.63

The cursors in Fig. 9 indicate a 35.62 % drop in emf measured at the commutation instant ($\theta_d = \frac{\pi}{6}$) compared to the 32.9 % drop expected from Fig. 6. The extra 2.9 % drop expected from the FEM ($\chi = 70\%$) is because of an error introduced by the interpolation between rise angle data points when the interpole angle θ_{ip} is determined.

The extent of armature reaction is shown in Fig. 10. It shows the airgap flux density and its time integral for (a) a very small phase current and (b) a large phase current. The plateau of the airgap flux density measured in the middle of the airgap is noticeably tilted by the armature reaction flux. However, the peak-to-peak value of the flux density's time integral, which is proportional to flux per pole, shows only a 3% decrease from 41.25 mVs to 40 mVs. The armature reaction effect therefore causes only a small reduction in average torque through saturation of the core.

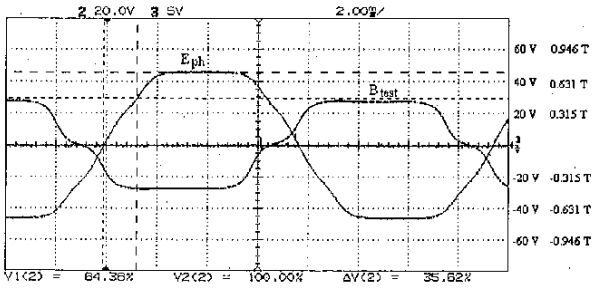

Fig. 9. Open Circuit Airgap Flux Density & Phase Emf

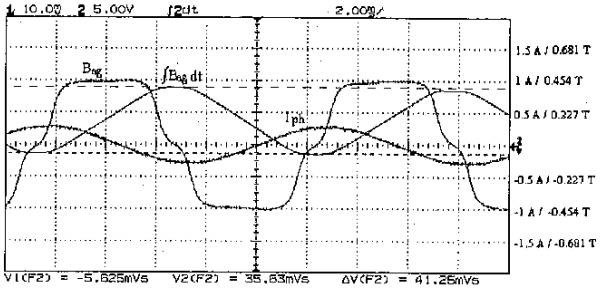

(a) Small Phase Current

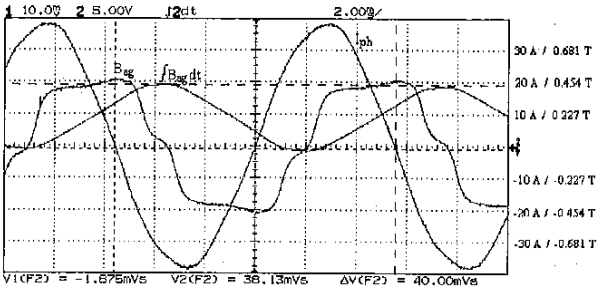

(b) Large Phase Current

Fig. 10. Armature Reaction Effect

Note that Fig. 10 illustrates the armature reaction effect for the quasi-sinusoidal phase currents flowing in the star connected load. For brushless DC motor operation the flux density shape will be somewhat different as a DC phase current is then conducted.

The thermal capacity of the machine is measured by conducting 26.8 A_{rms} at 1380 rpm for an extended period through the three phases. Ignoring the skin effect, the copper losses are then equal to that when 32.8 A DC flows in two phases. An average stator phase resistance increase of 7% was measured. This implies a copper temperature increase of 18° C. A temperature sensor recorded an increase of 14° C on the stator surface.

At 26.8 A_{rms} phase current and 1380 r/min, the torque is measured as 28.2 Nm and the power dissipated in the load is measured as 3496 W. Stator copper losses are estimated at 295 W. There are no core losses. Because copper losses are already at rated value, a very high efficiency will be obtained at high speed if the wind and friction losses can be contained.

B. Motor Operation

The AFPM machine was tested under speed and current control in brushless DC motor operation. A bipolar PWM switching scheme was used. The shaft torque was measured as 28.0 Nm at a current amplitude of 33 A. Fig. 11 shows the torque ripple measured at a shaft speed of 97 r/min. This speed was selected because mechanical resonances were found to be at a minimum there. The ripple frequency of 38.5 Hz in Fig. 11 corresponds to the frequency at which 60° electric cycles occur at 97 r/min.

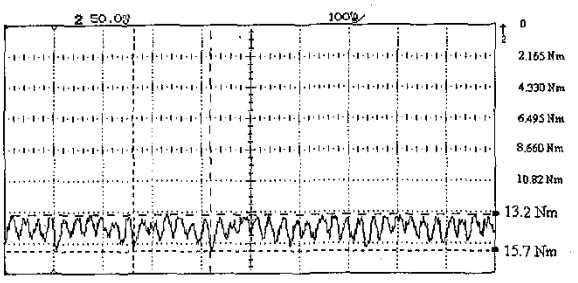

Fig. 11. Torque Ripple under Current Control

At most one active phase undergoes an emf dip at a time. The emf dips of 32.9% computed by the FEM and 35.6% measured in generator mode therefore translates to an expected torque ripple of 16.5% and 17.8% respectively under current control. This compares well to the measurement in Fig. 11, where the torque ripple amplitude is 16% of the peak value of torque.

V. Conclusions

The lumped circuit model is able to calculate the airgap flux density in the middle of a pole very accurately. The FEM predicts the shapes of the airgap flux density and emf waveforms satisfactory.

The use of interpolated data to obtain the magnet pitch instead of calling the FEM directly introduces a small error in the expected maximum emf dip (2.9 percentage points in the case study). However, during each iteration of the optimization process an interpolation is done instead of a FEM analysis.

Because the reduction of flux per pole due to armature reaction is small, a good prediction of the average torque may be made from the open circuit emf waveform. The modification of airgap flux density in the middle of the airgap does not cause a large increase in torque ripple.

Conservative dimensions were chosen for the machine's supporting sections in order to withstand the axial magnetic forces. This caused a large machine mass and consequently a low torque per mass of around 1 Nm per kg. The total magnet mass was 2.8 kg. The prototype machine displayed the expected characteristics of low noise, zero cogging torque and reduced copper losses for a certain power level at the expense of a large magnet volume.

VI. References

[1] Spooner, E., Chalmers, B.J.: "Torus: A Slotless Toroidal-Stator Permanent Magnet Generator", IEE Proc. B, 1992, Vol. 139, No. 6, pp. 497-506.

[2] Caricchi, F., Crescimbini, F.: "Design and Construction of a Wheel-Directly Coupled Axial-Flux PM Motor for EVs", IEEE IAS, 1994, pp. 254-261.

[3] Zhang, Z., Profumo, F.: "Axial Flux Wheel Machines for Electric Vehicles", Electric Machines and Power Systems Journal, Vol. 24, pp. 883-896.

[4] Caricchi, F., Crescimbini, F.: "Low-cost compact PM machine for adjustable-speed pump application", IEEE IAS, 1996, Vol. 1, pp. 464-470.

[5] Caricchi, F., Crescimbini, F., Mezetti, F., Santini, E.: "Multi-Stage Axial-Flux PM Machine for Wheel Direct Drive", IEEE IAS, 1995, pp. 679-684.

[6] Hoole, S. R.: "Computer Aided Design of Electromagnetic devices", 1989, Elsevier Science Publishing Co. Inc., New York.

[7] Press, W. H.: "Numerical Recipies", 1986, Cambridge University Press, Cambridge.

[8] Lombard, N. F.: "Design and Evaluation of an Ironless Stator Axial Flux PM Machine", M. Eng. thesis, University of Stellenbosch, 1997.

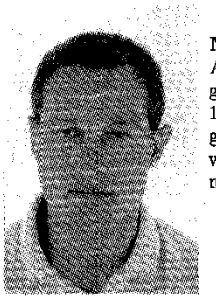

Nicolas F. Lombard was born in South Africa in 1973. He received the B.Eng. degree from the University of Stellenbosch in 1995. He recently completed the M.Eng. degree at the University of Stellenbosch, for which he has done research on brushless DC machines.

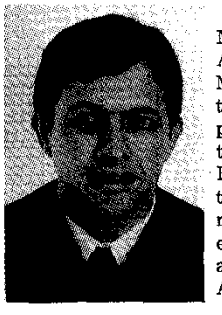

Maarten J. Kamper was born in South Africa in 1959. He received the B.Eng. ('83), M.Eng. ('87) and PhD. ('96) degrees from the University of Stellenbosch. He was employed by the SA Transport Services and the SA Council for Scientific and Industrial Research. He joined the lecturing staff of the University of Stellenbosch in 1989. His main interests are electrical machines, power electronics and variable speed drives. He is a registered professional engineer in South Africa.